Numer Algor (2018) 78:513–533
DOI 10.1007/s11075-017-0386-x

ORIGINAL PAPER

Speckle noise removal in ultrasound images by first- and second-order total variation

Si Wang[1] · Ting-Zhu Huang[2] · Xi-Le Zhao[2] · Jin-Jin Mei[2] · Jie Huang[2]

Received: 30 October 2016 / Accepted: 30 July 2017 / Published online: 12 August 2017

Abstract Speckle noise contamination is a common issue in ultrasound imaging system. Due to the edge-preserving feature, total variation (TV) regularization-based techniques have been extensively utilized for speckle noise removal. However, TV regularization sometimes causes staircase artifacts as it favors solutions that are piecewise constant. In this paper, we propose a new model to overcome this deficiency. In this model, the regularization term is represented by a combination of total variation and high-order total variation, while the data fidelity term is depicted by a generalized Kullback-Leibler divergence. The proposed model can be efficiently solved by alternating direction method with multipliers (ADMM). Compared with some state-of-the-art methods, the proposed method achieves higher quality in terms of the peak signal to noise ratio (PSNR) and the structural similarity index (SSIM).

✉ Ting-Zhu Huang
tingzhuhuang@126.com

Si Wang
uestcsiwang@163.com

Xi-Le Zhao
xlzhao122003@163.com

Jin-Jin Mei
meijinjin666@126.com

Jie Huang
happyjie07mo@163.com

1 School of Computer Science and Engineering, University of Electronic Science and Technology of China, Chengdu, 611731, Sichuan, People's Republic of China

2 School of Mathematical Sciences, University of Electronic Science and Technology of China, Chengdu, 611731, Sichuan, People's Republic of China

Numerical experiments demonstrate that our method can remove speckle noise efficiently while suppress staircase effects on both synthetic images and real ultrasound images.

Keywords Speckle noise · Total variation · High-order total variation · Alternating direction method with multipliers · Generalized Kullback-Leibler divergence · Ultrasound images

1 Introduction

Ultrasonography is a widely used diagnostic technique, due to its noninvasive nature, low cost, safety, portability, and capability of forming real-time imaging [1, 14]. Unfortunately, ultrasound images show a granular appearance called speckle, which degrades visual evaluations. Hence, it becomes difficult for human to distinguish normal and pathological tissue in diagnostic examinations [23]. Ultrasonic speckle is an interference effect caused by the scattering of the ultrasonic beam from microscopic tissue inhomogeneities [33]. It tends to obfuscate some important image features and reduce the image contrast. Therefore, speckle noise removal is an important task in medical ultrasound imaging processing [10, 38]. Mathematically, the speckle noise can be modeled by the following multiplicative form:

$$f = un, \tag{1}$$

where the degraded image f, the original image u and the speckle noise n are functions from Ω to $\mathbb{R}_+$ with $\Omega \in \mathbb{R}^2$ [48]. Because of its multiplicative nature and its distribution is generally not Gaussian, it is difficult to remove multiplicative noise [46].

Many approaches have been proposed to suppress speckle noise, such as local statistics [26, 31], anisotropic diffusion approaches [25, 54], nonlocal filtering approaches [8, 9, 41], and variational approaches [19, 20, 22, 56]. Variational approaches have drawn great attention for speckle noise removal. The variational model consists of a data fidelity term and a regularization term. Total variation (TV) has been widely used as a regularizer in processing of speckle noise due to its ability to preserve sharp discontinuities in restored images [28, 45, 47]. In the following, we briefly review some TV-based methods.

To the best of our knowledge, the first TV regularizer-based method which devoted to remove multiplicative noise is proposed by Rudin, Lions, and Osher (RLO model) [43]. The RLO model is given by

$$\min_{u\in BV(\Omega)} \int_\Omega |Du| \quad \text{s.t.} \int_\Omega u dx = \int_\Omega u_0 dx, \quad \frac{1}{|\Omega|}\int_\Omega (\frac{f}{u}-1)^2 dx = \sigma^2, \tag{2}$$

where $\Omega \subset \mathbb{R}^2$ denotes an open bounded set, $BV(\Omega)$ denotes the space of functions with bounded variation on Ω, $\int_\Omega |Du|$ is the total variation of u, $|\Omega|$ denotes the area of Ω, and σ is the standard deviation of the noise. This approach is very effective to remove multiplicative noise that follows Gaussian distribution. However, Tur, Chin and Goodman found that the speckle noise can be approximated by Rayleigh distribution when the scatter density was more than 10 [49]. Due to the signal processing stages inside the scanner (logarithmic compression, interpolation), Loupas, Mcdicken, and Allan show that the speckle noise is not in a multiplicative form in ultrasound imaging [32, 33]. They indicate that the mean is proportional to the variance. Therefore, the displayed ultrasonic images can be modeled as the following form:

$$f = u + \sqrt{u}n, \tag{3}$$

where f is the observed image, u is the original image and n is a zero-mean Gaussian noise with the variance σ^2 [24]. This model fits better than multiplicative model (1) for ultrasound images. Based on model (3), some approaches have been proposed to remove the speckle noise. In [22], the authors propose the following variational model:

$$\min_{u \in BV(\Omega)} \int_\Omega |Du| + \lambda \int_\Omega \frac{(f-u)^2}{u} dx, \tag{4}$$

which is solved by a gradient projection method. They prove the existence and uniqueness of the minimizer. It should be noted that the performance of this method depends on the accuracy of the estimated noise variance. In [19], the authors propose a convex variational model which combines the Kullback-Leibler divergence data fidelity term and total variation regularization term to remove speckle noise. By denoting $z = \log u$, the model is given by

$$\min_{z \in BV(\Omega)} \int_\Omega |Dz| + \lambda \int_\Omega \left(f e^{-z/2} \log \frac{f}{e^z} - f e^{-z/2} + e^{z/2} \right) dx, \tag{5}$$

which is solved by split Bregman iteration method. This method can preserve sharp edges and suppress speckle noise efficiently.

Since TV regularizer transforms smooth regions into piecewise constant ones, it often produces staircase artifacts. These artifacts fail to satisfy the visual evaluation and they may develop false edges which do not exist in the true image. Several high-order methods are proposed to reduce the artifacts for additive noise [3, 5, 27, 29, 34, 44, 53]. In [5], the authors consider a high-order method through an inf-convolution of a first order functional and a second-order functional. The authors in [29] propose a noise removal method which combines a TV filter with a fourth-order partial differential equations filter. These methods alleviate the staircase effects of TV denoising methods while preserving discontinuous as well as TV denoising methods. Motivated by the advantage of high-order total variation for the additive noise removal, we propose a convex model consisting of the Kullback-Leiber divergence as the data fidelity term, the total variation regularization, and high-order total variation regularization terms. As the proposed model is a convex problem, there are many efficient methods to solve it, such as split Bregman method, primal-dual method, Douglas-Rachford spltting method, and alternating direction method with multipliers (ADMM). In this work, ADMM is developed to solve the proposed model.

The remainder of this paper is organized as follows. In Section 2, we propose our model for despeckling in ultrasound imaging. In Section 3, we develop an efficient ADMM scheme to solve the proposed model. Numerical results are reported to show the effectiveness of the proposed method in Section 4. Finally, some concluding remarks are given in Section 5.

2 The proposed speckle noise removal model

In this section, we start with a brief review of the generalized Kullback-Leibler divergence and high-order total variation [4, 29, 40]. In probability theory and information theory, Kullback-Leibler divergence is a discrepancy measure of the difference between two probability distribution, which has been widely used in image processing [2, 19, 36, 42, 47].

Definition 2.1 Let $S = \mathbb{R}_{+}^{N}$, the Kullback-Leibler divergence (also called as I-divergence) of $f \in S$ from $u \in S$ is defined by

$$I(f||u) = \sum_{i=1}^{N} \left(f_i \log \frac{f_i}{u_i} - f_i + u_i \right). \tag{6}$$

Definition 2.2 Let $\Omega \subset \mathbb{R}^n$ be an open subset with Lipschitz boundary. Define $BV(\Omega)$ as a subspace of functions $u \in L^1(\Omega)$ such that the following quantity

$$\int_{\Omega} |Du| := \sup \left\{ \int_{\Omega} u \mathrm{div}(\varphi) dx | \varphi \in C_c^1(\Omega, R^n), |\varphi| \leq 1 \right\} \tag{7}$$

is finite. $BV(\Omega)$ is a Banach space with the norm $\|u\|_{BV(\Omega)} = \int_{\Omega} |Du| + \|u\|_{L^1(\Omega)}$[37].

Definition 2.3 Let $\Omega \subset \mathbb{R}^n$ be an open subset with Lipschitz boundary. Define $BV^2(\Omega)$ as a subspace of functions $u \in L^1(\Omega)$ such that the following quantity

$$\int_{\Omega} |D^2 u| := \sup \left\{ \int_{\Omega} \sum_{i,j=1}^{n} u \partial_j \partial_i \varphi^{ij} dx | \varphi \in C_c^2(\Omega, R^{n\times n}), |\varphi| \leq 1 \right\} \tag{8}$$

is finite, where $|\varphi(x)| = \sqrt{\sum_{i=1}^{n} \sum_{j=1}^{n} (\varphi^{ij})^2}$. $BV^2(\Omega)$ is a Banach space with the norm $\|u\|_{BV^2(\Omega)} = \int_{\Omega} |D^2 u| + \|u\|_{L^1(\Omega)}$.

As described in the literature [29], we introduce the weighted BV^2 space denoted by $\beta - BV^2(\Omega)$. A function u belongs to $\beta - BV^2(\Omega)$ if $u \in L^1(\Omega)$ and satisfies

$$\int_{\Omega} \beta |D^2 u| := \sup \left\{ \int_{\Omega} \sum_{i,j=1}^{n} u \partial_j \partial_i \varphi^{ij} dx | \varphi \in C_c^2(\Omega, R^{n\times n}), |\varphi| \leq \beta \right\} < \infty,$$

where β is a nonnegative function.

In the following, we design our speckle removal model for ultrasound images. From (3), we get

$$\frac{f}{\sqrt{u}} = \sqrt{u} + n. \tag{9}$$

By using the definition of Kullback-Leibler divergence, we obtain the following data fidelity term:

$$I\big(\frac{f}{\sqrt{u}}||\sqrt{u}\big) = \int_\Omega \big(\frac{f}{\sqrt{u}}\log\frac{f}{u} - \frac{f}{\sqrt{u}} + \sqrt{u}\big)dx, \tag{10}$$

which measures the discrepancy between the observed image and the original image. Motivated by the advantage of high-order TV, we combine TV and high-order TV as regularization term and get the following model:

$$\min_u \lambda \int_\Omega \big(\frac{f}{\sqrt{u}}\log\frac{f}{u} - \frac{f}{\sqrt{u}} + \sqrt{u}\big)dx + \int_\Omega \alpha|Du| + \int_\Omega \beta|D^2u|, \tag{11}$$

where α and β are weighted functions. The objective function of (11) is not convex for all u. The computed solutions of (11) by some optimization methods may not be globally optimal. To address this issue, we adopt the strategy proposed in [20] by taking $z = \log u$ as u and z contain an edge at the same location. We can view z as an image in the logarithm domain. By applying TV and high-order TV to z, we arrive at our speckle removal model for ultrasound images:

$$\min_z \lambda \int_\Omega (fe^{-z/2}\log\frac{f}{e^z} - fe^{-z/2} + e^{z/2})dx + \int_\Omega \alpha|Dz| + \int_\Omega \beta|D^2z|. \tag{12}$$

It is easy to see that when $\alpha(x) = 1$ and $\beta(x) = 0$, our proposed model is identified with model (5). Thus our model is expected to keep sharp edges like model (5). Besides, our model efficiently combines the advantage of the TV denosing model and high-order TV denoising model. This combined technique is able to preserve edges while reducing staircase effects in smooth regions.

We now show that the function (12) is strictly convex; hence, the global optimal solution is guaranteed. Let

$$g(z) = fe^{-z/2}\log\frac{f}{e^z} - fe^{-z/2} + e^{z/2},$$

it is easy to obtain the derivative of $g(z)$,

$$g'(z) = -\frac{1}{2}fe^{-z/2}\log f + \frac{1}{2}fe^{-z/2}z - \frac{1}{2}fe^{-z/2} + \frac{1}{2}e^{z/2},$$

and the second-order derivative

$$g''(z) = \frac{1}{4}fe^{-z/2}(e^z/f + \log f + 3 - z).$$

When $z = \log(f)$, $e^z/f + \log f + 3 - z$ attains its minimizer. Therefore,

$$e^z/f + \log f + 3 - z \geq e^{\log f}/f + \log f + 3 - \log f = 4 > 0.$$

Note that $\frac{1}{4}fe^{-z/2}$ is always positive when $f > 0$, then $g''(z) > 0$ when $f > 0$, implying that $g(z)$ is strictly convex for all z. Consequently, the proposed objective function (12) is strictly convex. Then, the existence and uniqueness of the minimizer of problem (12) is guaranteed based on the discussion in [19].

3 Numerical algorithm

In the following, we develop the alternating direction method of multipliers (ADMM) to solve (12). Firstly, we briefly review ADMM [13, 16–18, 21, 30, 50]. The ADMM solves the following linear separable convex minimization problem of the form:

$$\begin{aligned} &\min\ \theta_1(x_1)+\theta_2(x_2),\\ &s.t.\quad A_1x_1+A_2x_2=b,\\ &x_1\in\Omega_1\ \text{ and }\ x_2\in\Omega_2, \end{aligned} \tag{13}$$

where $\theta_1:\mathbb{R}^{n_1}\to\mathbb{R}$ and $\theta_2:\mathbb{R}^{n_2}\to\mathbb{R}$ are closed proper convex functions, $\Omega_1\subseteq\mathbb{R}^{n_1}$ and $\Omega_2\subseteq\mathbb{R}^{n_2}$ are closed convex sets, $A_1\in\mathbb{R}^{l\times n_1}$ and $A_2\in\mathbb{R}^{l\times n_2}$ are given matrices, and $b\in\mathbb{R}^l$ is a given vector. The augmented Lagrangian function of (13) is

$$L(x_1,x_2,d)=\theta_1(x_1)+\theta_2(x_2)+\frac{\mu}{2}\|(A_1x_1+A_2x_2-b)-d\|^2.$$

In the framework of ADMM, the optimization problem of (13) can be efficiently solved by the following algorithm:

Algorithm ADMM

1. Set $k=0$. Choose $\mu>0$. Initialize x_2^0 and d^0.
2. Calculate x_1^{k+1}, x_2^{k+1} and d^{k+1} using the following equations:
$$\begin{aligned} x_1^{k+1}&=\arg\min_{x_1}\{L(x_1,x_2^k,d^k)\mid x_1\in\Omega_1\},\\ x_2^{k+1}&=\arg\min_{x_2}\{L(x_1^k,x_2,d^k)\mid x_2\in\Omega_2\},\\ d^{k+1}&=d^k-(A_1x_1^{k+1}+A_2x_2^{k+1}-b). \end{aligned}$$
3. Stop or set $k:=k+1$ and go back to step 2.

The convergence proof of ADMM and its variants can be found in [11, 16]. In many cases, we can not get the exact solutions of subproblems x_1 and x_2. The convergence of the algorithm is also guaranteed as long as the sequences of optimization errors with respect to x_1 and x_2 are absolutely summable [11].

In the following, we present our algorithm for solving the proposed model. Since we deal with the discrete formulation of the image, we consider the discrete form of (12). To begin, we introduce some basic notations. Assume $S=\{(i,j)|i=1,2,\cdots,m,\ j=1,2,\cdots,n\}$ is the discrete grid of the image domain, without loss of generality, we represent a grayscale image as an $m\times n$ matrix. The Euclidean space $\mathbb{R}^{m\times n}$ is denoted as V. The discrete gradient operator is a mapping $\nabla:V\to Q$, where $Q=V\times V$ and the second-order difference operator ∇^2 is a mapping $\nabla^2:V\to Q_1$, where $Q_1=V\times V\times V\times V$. We refer the readers to [52] for more details about the first and second order difference operators. Then, the discrete version of (12) can be shown as follows:

$$\min_z \lambda\sum_{(i,j)\in S}g(z_{i,j})+\sum_{(i,j)\in S}\alpha_{i,j}\|(\nabla z)_{i,j}\|_2+\sum_{(i,j)\in S}\beta_{i,j}\|(\nabla^2 z)_{i,j}\|_2, \tag{14}$$

where

$$g(z_{i,j}) = f_{i,j}e^{-z_{i,j}/2}\log\frac{f_{i,j}}{e^{z_{i,j}}} - f_{i,j}e^{-z_{i,j}/2} + e^{z_{i,j}/2},$$

$$\|(\nabla z)_{i,j}\|_2 = \sqrt{((D_x^+ z)_{i,j})^2 + ((D_y^+ z)_{i,j})^2},$$

and

$$\|(\nabla^2 z)_{ij}\|_2 = \sqrt{((D_{xx}^{-+} z)_{i,j})^2 + ((D_{xy}^{++} z)_{i,j})^2 + ((D_{yx}^{++} z)_{i,j})^2 + ((D_{yy}^{-+} z)_{i,j})^2}.$$

Here, we use D_x^+ and D_y^+ to denote forward difference operators with periodic boundary condition, and D_x^- and D_y^- to denote backward difference operators with periodic boundary condition (z is periodically extended). It should be mentioned that some other boundary conditions and corresponding definitions of ∇ and ∇^2 can be used [15, 39]. For any $z \in \mathbb{R}^{m\times n}$, we define $(\nabla z)_{i,j} := ((D_x^+ z)_{i,j}, (D_y^+ z)_{i,j})$, $(\nabla^2 z)_{i,j} := \begin{pmatrix} (D_{xx}^{-+} z)_{i,j} & (D_{xy}^{++} z)_{i,j} \\ (D_{yx}^{++} z)_{i,j} & (D_{yy}^{-+} z)_{i,j} \end{pmatrix}$, with

$$(D_x^+ z)_{i,j} = \begin{cases} z_{i,j+1} - z_{i,j}, & 1 \leqslant j \leqslant n-1, \\ z_{i,1} - z_{i,n}, & j = n, \end{cases}$$

$$(D_y^+ z)_{i,j} = \begin{cases} z_{i+1,j} - z_{i,j}, & 1 \leqslant i \leqslant m-1, \\ z_{1,j} - z_{m,j}, & i = m, \end{cases}$$

$$(D_x^- z)_{i,j} = \begin{cases} z_{i,j} - z_{i,j-1}, & 2 \leqslant j \leqslant n, \\ z_{i,1} - z_{i,n}, & j = 1, \end{cases}$$

$$(D_y^- z)_{i,j} = \begin{cases} z_{i,j} - z_{i-1,j}, & 2 \leqslant i \leqslant m, \\ z_{1,j} - z_{m,j}, & i = 1, \end{cases}$$

$$(D_{xx}^{-+} z)_{i,j} := (D_x^-(D_x^+ z))_{i,j},$$
$$(D_{xy}^{++} z)_{i,j} := (D_x^+(D_y^+ z))_{i,j},$$
$$(D_{yx}^{++} z)_{i,j} := (D_y^+(D_x^+ z))_{i,j},$$
$$(D_{yy}^{-+} z)_{i,j} := (D_y^-(D_y^+ z))_{i,j}.$$

For every $z \in \mathbb{R}^{m\times n}$, $p = (p^1, p^2) \in Q$ and $q = \begin{pmatrix} q^1 & q^2 \\ q^3 & q^4 \end{pmatrix} \in Q_1$, we define

$$\|z\|_2 = \left(\sum_{i=1}^m \sum_{j=1}^n (z_{i,j})^2\right)^{1/2},$$

$$\|p\|_2 = \left(\sum_{i=1}^m \sum_{j=1}^n (p_{i,j}^1)^2 + (p_{i,j}^2)^2\right)^{1/2},$$

$$\|q\|_2 = \left(\sum_{i=1}^m \sum_{j=1}^n (q_{i,j}^1)^2 + (q_{i,j}^2)^2 + (q_{i,j}^3)^2 + (q_{i,j}^4)^2\right)^{1/2}.$$

Then, we reformulate (14) as the following equivalent constrained problem:

$$\begin{aligned} &\min_{z,w,p,q} \lambda \sum_{(i,j)\in S} g(w_{i,j}) + \sum_{(i,j)\in S} \alpha_{i,j}\|p_{i,j}\|_2 + \sum_{(i,j)\in S} \beta_{i,j}\|q_{i,j}\|_2, \\ &\quad s.t. \quad w = z,\, p = \nabla z,\, q = \nabla^2 z, \end{aligned} \tag{15}$$

where $\|p_{i,j}\|_2 = \sqrt{(p^1_{i,j})^2 + (p^2_{i,j})^2}$, and $\|q_{i,j}\|_2 = \sqrt{(q^1_{i,j})^2 + (q^2_{i,j})^2 + (q^3_{i,j})^2 + (q^4_{i,j})^2}$.

We now show that the model (15) can be reformulated into

$$\begin{aligned} &\min \ \theta_1(x_1) + \theta_2(x_2), \\ &s.t. \quad A_1x_1 + A_2x_2 = b. \end{aligned}$$

Define the two $m \times m$ banded circulant matrices $D_{1,m}$ and $D_{2,m}$ by

$$D_{1,m} = \begin{pmatrix} -1 & 1 & & & 0 \\ 0 & -1 & 1 & & \\ & \ddots & \ddots & \ddots & \\ & & 0 & -1 & 1 \\ 1 & & & 0 & -1 \end{pmatrix},$$

$$D_{2,m} = \begin{pmatrix} 1 & 0 & & & -1 \\ -1 & 1 & 0 & & \\ & \ddots & \ddots & \ddots & \\ & & -1 & 1 & 0 \\ 0 & & & -1 & 1 \end{pmatrix},$$

then $D_y^+ z = D_{1,m}z$, $D_x^+ z = zD_{1,n}^T$, $D_y^- z = D_{2,m}z$, $D_x^- z = zD_{2,n}^T$. Let $x_1 = vec(z) \in \mathbb{R}^{mn}$,

$$x_2 = \Big((vec(w))^T, (vec(p^1))^T, (vec(p^2))^T, (vec(q^1))^T, (vec(q^2))^T, (vec(q^3))^T, (vec(q^4))^T\Big)^T \in \mathbb{R}^{7mn},$$

$\theta_1(x_1) = 0$, $\theta_2(x_2) = \lambda \sum_{(i,j)\in S} g(w_{i,j}) + \sum_{(i,j)\in S} \alpha_{i,j}\|p_{i,j}\|_2 + \sum_{(i,j)\in S} \beta_{i,j}\|q_{i,j}\|_2$, then (15) can be reformulated into

$$\begin{aligned} &\min_{x_1,x_2} \theta_1(x_1) + \theta_2(x_2) \\ &s.t. \begin{pmatrix} I_{mn} \\ D_{1,n} \otimes I_m \\ I_n \otimes D_{1,m} \\ (D_{2,n}D_{1,n}) \otimes I_m \\ D_{1,n} \otimes D_{1,m} \\ D_{1,n} \otimes D_{1,m} \\ I_n \otimes (D_{2,m}D_{1,m}) \end{pmatrix} x_1 - x_2 = \mathbf{0}, \end{aligned}$$

where I_m denotes the identity matrix with size $m \times m$, and $\mathbf{0}$ denotes the zero vector with size $7mn \times 1$.

Remark: It is not necessary to construct the explicit matrices A_1 and A_2 in real application, some fast transforms can be applied to solve x_1-subproblem. Similar techniques are used in [6, 7, 15, 20, 40, 55, 56].

The corresponding augmented Lagrangian function of (15) is given by:

$$\begin{aligned} L(z, w, p, q, \mathbf{b}) = & \ \lambda \textstyle\sum_{(i,j)\in S} g(w_{i,j}) + \sum_{(i,j)\in S} \alpha_{i,j} \|p_{i,j}\|_2 + \sum_{(i,j)\in S} \beta_{i,j} \|q_{i,j}\|_2 \\ & + \tfrac{\mu}{2} \|w - z - d_1\|_2^2 \\ & + \tfrac{\mu}{2} \|p - \nabla z - d_2\|_2^2 + \tfrac{\mu}{2} \|q - \nabla^2 z - d_3\|_2^2, \end{aligned}$$

where $d_1 \in \mathbb{R}^{m\times n}$, $d_2 \in Q$, $d_3 \in Q_1$, and $\mu > 0$ is a penalty parameter to control the speed of convergence [40]. The variables w, p, q, z can be separated into two groups, (w, p, q) and z. For a fixed value of z, the variables w, p, q are decoupled. Then, we can solve them on their corresponding subproblems by ADMM. The iterative scheme of (15) is given by

$$\begin{cases} z^{k+1} = \arg\min\limits_{z} \dfrac{\mu}{2} \|z + d_1^k - w^k\|_2^2 + \dfrac{\mu}{2} \|\nabla z + d_2^k - p^k\|_2^2 + \dfrac{\mu}{2} \|\nabla^2 z + d_3^k - q^k\|_2^2, \\ w^{k+1} = \arg\min\limits_{w} \lambda \sum\limits_{(i,j)\in S} g(w_{ij}) + \dfrac{\mu}{2} \|w - z^{k+1} - d_1^k\|_2^2, \\ p^{k+1} = \arg\min\limits_{p} \sum\limits_{(i,j)\in S} \alpha_{i,j} \|p_{i,j}\|_2 + \dfrac{\mu}{2} \|p - \nabla z^{k+1} - d_2^k\|_2^2, \\ q^{k+1} = \arg\min\limits_{p} \sum\limits_{(i,j)\in S} \beta_{i,j} \|q_{i,j}\|_2 + \dfrac{\mu}{2} \|q - \nabla^2 z^{k+1} - d_3^k\|_2^2, \\ d_1^{k+1} = d_1^k - (w^{k+1} - z^{k+1}), \\ d_2^{k+1} = d_2^k - (p^{k+1} - \nabla z^{k+1}), \\ d_3^{k+1} = d_3^k - (q^{k+1} - \nabla^2 z^{k+1}). \end{cases} \tag{16}$$

For the z-subproblem, we obtain

$$\left(I + \nabla^T \nabla + (\nabla^2)^T \nabla^2\right) z^{k+1} = w^k - d_1^k + \nabla^T (p^k - d_2^k) + (\nabla^2)^T (q^k - d_3^k). \tag{17}$$

As ∇ and ∇^2 are the first-order and the second-order difference operators respectively, the coefficient matrix associated with z can be diagonalized by some fast transforms. Since we impose periodic boundary condition for the discrete scheme, the z-subproblem can be solved efficiently by fast Fourier transform. For more details, we refer the reader to [15, 39].

The minimization of w in (16) is a set of $m \times n$ decoupled scalar convex minimizations. Since the objective function $F(w_{i,j}) = \lambda g(w_{i,j}) + \frac{\mu}{2}(w_{i,j} - z_{i,j} - d_{1_{i,j}})^2$ is strictly convex, the solution of w is unique. The w-subproblem can be solved by Newton method efficiently. An iterative scheme of w is

$$w_{M+1}^{k+1} = w_M^{k+1} - \frac{F'(w_M^{k+1})}{F''(w_M^{k+1})}, \tag{18}$$

where M is the number of inner iteration of Newton method. In the numerical experiments, we set $M = 2$. We will discuss about the choice of inner iteration number in more details in Section 4.

As the p-subproblem is componentwise separable, the solution of p is

$$p_{i,j}^{k+1} = \text{shrink}\big((\nabla z^{k+1} + d_2^k)_{i,j}, \frac{\alpha_{i,j}}{\mu}\big), \quad (i, j) \in S, \tag{19}$$

where $p_{i,j}^{k+1} \in \mathbb{R}^2$ represents the component of p^{k+1} located at $(i, j) \in S$, and the shrinkage operator is defined by

$$\text{shrink}(t, \alpha) = \begin{cases} \mathbf{0}, & t = \mathbf{0}, \\ (\|t\|_2 - \alpha)\frac{t}{\|t\|_2}, & t \neq \mathbf{0}. \end{cases}$$

For the q-subproblem, the solution is

$$q_{i,j}^{k+1} = \text{shrink}\big((\nabla^2 z^{k+1} + d_3^k)_{i,j}, \frac{\beta_{i,j}}{\mu}\big), \quad (i, j) \in S, \tag{20}$$

where $q_{i,j}^{k+1} \in \mathbb{R}^{2\times 2}$ represents the component of q^{k+1} located at $(i, j) \in S$.

In summary, the proposed alternating direction method for ultrasound speckle removal is given as follows.

Algorithm The proposed speckle removal method

1. Choose $\lambda > 0, \alpha > 0, \beta > 0, \mu > 0$ and tolerance error $\epsilon > 0$. Initialize w^0, p^0, q^0, d_1^0, d_2^0, d_3^0.
2. Iteration:

   z^{k+1} is given by (17),
   w^{k+1} is given by (18),
   p^{k+1} is given by (19),
   q^{k+1} is given by (20),
   $d_1^{k+1} = d_1^k - (w^{k+1} - z^{k+1})$,
   $d_2^{k+1} = d_2^k - (p^{k+1} - \nabla z^{k+1})$,
   $d_3^{k+1} = d_3^k - (q^{k+1} - \nabla^2 z^{k+1})$,
   then, the restoration image u is $u^{k+1} = e^{z^{k+1}}$,

until $\|u^{k+1} - u^k\|_2/\|u^k\|_2 < \epsilon$.

4 Numerical results

In this section, some numerical experiments of the proposed method on both synthetic images and real ultrasound images are presented. We compare our method with some state-of-the-art TV based speckle removal algorithms introduced in [19, 22], and the I-divergence model with TGV regularization proposed in [12]. For simplicity, we call the method proposed in [12, 19, 22], as PDTGV-Idiv, FRSNU, RMNU, separately. For quantitative comparison, the peak signal to noise ratio (PSNR) and the structural similarity index (SSIM) [51] are introduced to measure the quality of the restoration. The PSNR is calculated by

$$\mathrm{PSNR} = 10\log_{10}\frac{\mathrm{N}\times \mathrm{MAX}_{u^*}^2}{\|u-u^*\|_2^2},$$

where u^*, u, N and MAX_u are the ground truth image, the recovered image, the number of pixels of the image, and the maximum possible pixel value of the image, respectively. The SSIM which measures the structural detail similarity between u and u^* is defined by

$$\mathrm{SSIM}(u,u^*) = \frac{(2\mu_u\mu_{u^*})(2\sigma_{uu^*}+c_2)}{(\mu_u^2+\mu_{u^*}^2+c_1)(\sigma_u^2+\sigma_{u^*}^2+c_2)},$$

where μ_u and μ_{u^*} are the mean values of image u and u^*. σ_u and σ_{u^*} denote their standard deviations, and σ_{uu^*} is the covariance of u and u^*. Moreover, $c_1 = (K_1L)^2$ and $c_2 = (K_2L)^2$, where L is the dynamic range of the pixel intensities (255 for 8-bit gray-scale images). $K_1 \ll 1$ and $K_2 \ll 1$ are small constants. The range of SSIM value lies in [0,1] with 1 for the perfect quality. In the numerical experiments, we use the following parameter values: $K_1 = 0.001$ and $K_2 = 0.03$. All the algorithms are terminated when $\frac{\|u^{k+1}-u^k\|_2}{\|u^k\|_2} < 5\times 10^{-4}$ except RMNU. As the performance of RMNU depends on the estimation of noise variance, we stop RMNU when the variance of the recovered noise matches that of the prior knowledge as described in [22]. For a fair comparison among the competing methods, we have carefully tuned

Fig. 1 Six different test synthetic images used in our experiments. *Top left:* Zelda (512 × 512); *top middle:* Face (268 × 360); *top right:* House (512 × 512); *bottom left:* Pallon (256 × 256); *bottom middle:* Tulip (256 × 256); *bottom right:* Barche (256 × 256)

the parameters in RMNU, FRSNU, and PDTGV-Idiv for each image to give the best possible performance.

For our proposed method, we choose $x^0 = \mathbf{0}$, $p^0 = \mathbf{0}$, $q^0 = \mathbf{0}$, $d_1^0 = \mathbf{0}$, $d_2^0 = \mathbf{0}$, $d_3^0 = \mathbf{0}$. The data fidelity coefficient λ is related to noise levels. The larger the noise is, the smaller λ is. There are several methods to choose regularization parameters α and β, such as the methods proposed in [29, 35]. In [29], the authors suggest that the scheme of α and β can be choosen as

$$\alpha = \frac{\gamma + \eta|\nabla(G_\delta * f)|^2}{1 + \gamma + \eta|\nabla(G_\delta * f)|^2},$$

and

$$\beta = 1 - \alpha,$$

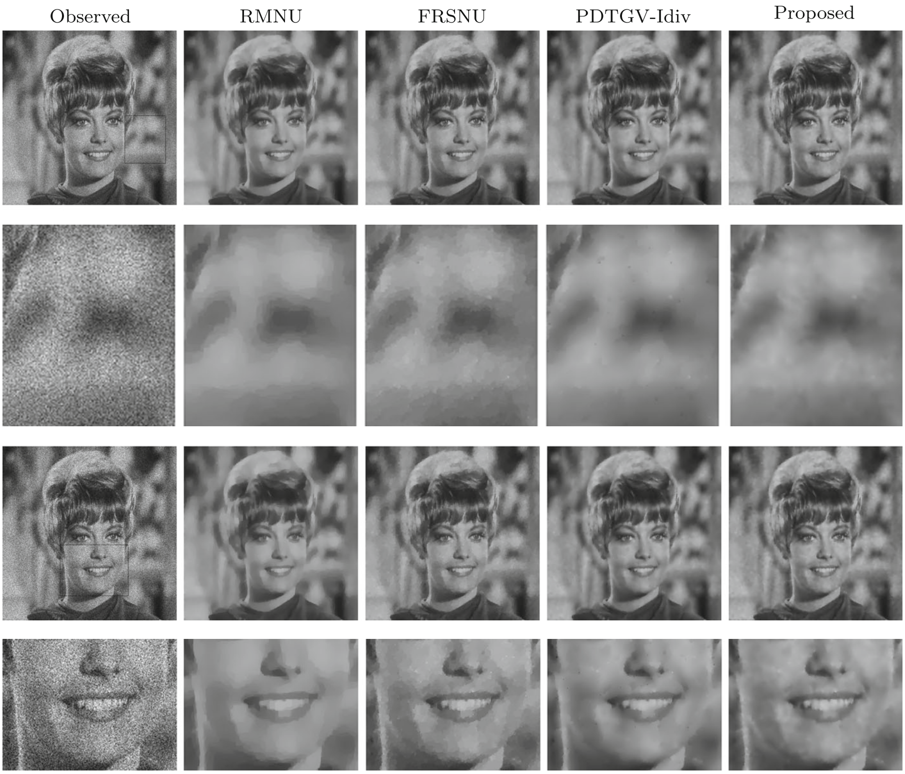

Fig. 2 *First row:* performance comparison of different methods on Zelda with $\sigma = 2$, *from left to right:* observed image, restored results by RMNU with $PSNR = 32.27dB$, FRSNU with $PSNR = 32.78dB$, PDTGV-Idiv with $PSNR = 33.19dB$, and the proposed method with $PSNR = 33.38dB$ ($\lambda = 0.8$, $\mu = 10$). *Second row:* corresponding zoomed-in regions in the first row. *Third row:* performance comparison of different methods on Flower with $\sigma = 3$, *from left to right:* observed image, restored results by RMNU with $PSNR = 29.90dB$, FRSNU with $PSNR = 31.07dB$, PDTGV-Idiv with $PSNR = 31.64dB$, and the proposed method with $PSNR = 31.46dB$ ($\lambda = 0.5$, $\mu = 10$). *Bottom row:* corresponding zoomed-in regions in the third row

where $\gamma > 0$ is a very small positive number, $\eta > 0$ is a contrast factor, G_δ is the Gaussian kernel, δ denotes the standard deviation, and $*$ is a convolution operator. We adopt this strategy to choose α and β in our numerical experiments by setting $\gamma = 0.0001$, $\eta = 0.01$ and $\delta = 2$. By this selection of α and β, $\alpha\|\nabla z\|$ tends to be predominant when $|\nabla(G_\delta * f)|$ is large (large $|\nabla(G_\delta * f)|$ corresponds to locations where the edges most likely to appear); and $\beta\|\nabla^2 z\|$ tends to be predominant when $|\nabla(G_\delta * f)|$ is small (small $|\nabla(G_\delta * f)|$ corresponds to locations with smooth areas). Thus the proposed model can preserve sharp edges and restore smooth regions well.

All simulations are implemented in MATLAB R2010a on a personal computer with a 2.80GHz Intel Pentium CPU and 4 Gb of RAM.

4.1 Experiments on synthetic images

In Fig. 1, six original synthetic images are presented and we denote them by Zelda, Face, House, Pallon, Tulip, and Barche, respectively.

Test 1 Figures 2, 3 and 4 present the restored results of the images Zelda, Face, and House corrupted by speckle noise with $\sigma = 2$ and $\sigma = 3$. From the despeckled

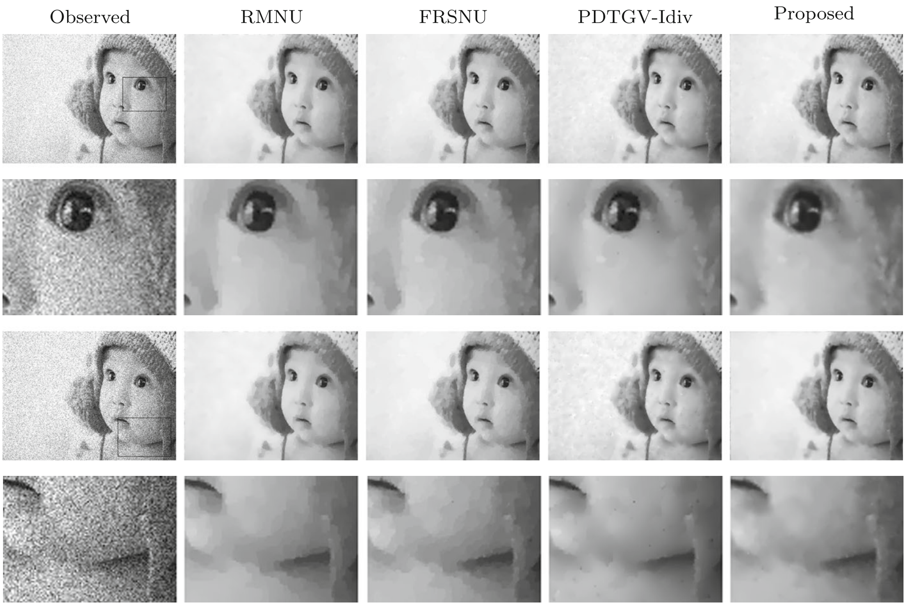

Fig. 3 *First row:* performance comparison of different methods on Face image with $\sigma = 2$, form *left to right:* observed image, restored results by RMNU with $PSNR = 31.13dB$, FRSNU with $PSNR = 31.35dB$, PDTGV-Idiv with $PSNR = 31.19dB$, and the proposed method with $PSNR = 31.61dB$ ($\lambda = 0.6$, $\mu = 70$). *Second row:* corresponding zoomed-in regions in the first row. *Third row:* performance comparison of different methods on Face image with $\sigma = 3$, *form left to right:* observed image, restored results by RMNU with $PSNR = 29.09dB$, FRSNU with $PSNR = 29.41dB$, PDTGV-Idiv with $PSNR = 29.12dB$, and the proposed method with $PSNR = 29.53dB$ ($\lambda = 0.3$, $\mu = 70$). *Bottom row:* corresponding zoomed-in regions in the third row

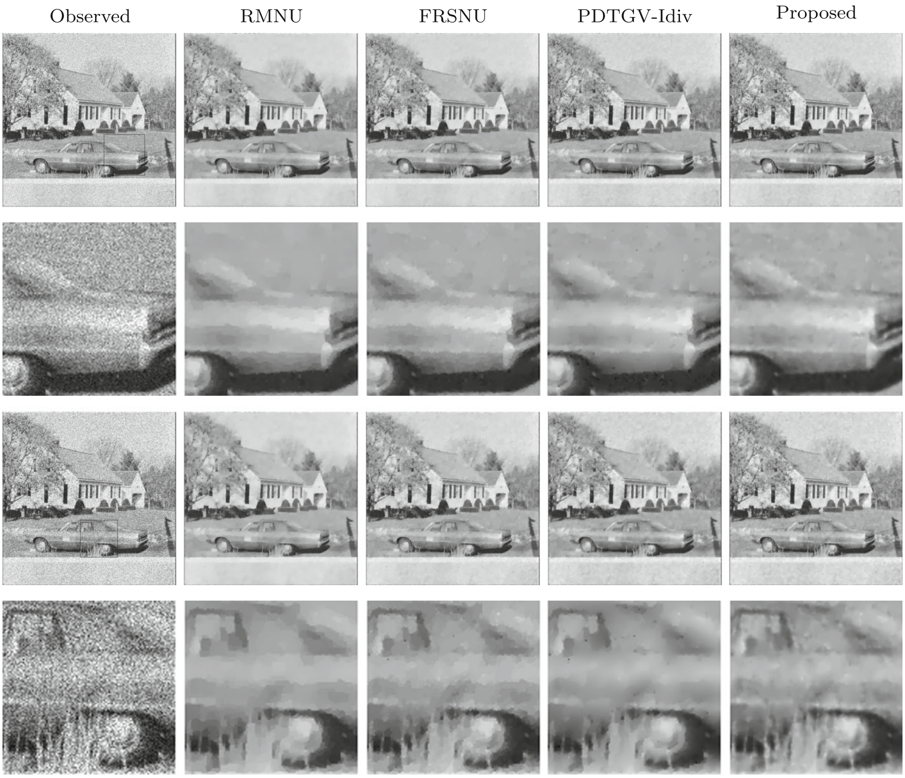

Fig. 4 *First row:* performance comparison of different methods on House with $\sigma = 2$, *from left to right:* observed image, restored results by RMNU with $PSNR = 28.15dB$, FRSNU with $PSNR = 28.35dB$, PDTGV-Idiv with $PSNR = 28.32B$, and the proposed method with $PSNR = 28.47dB$ ($\lambda = 0.8$, $\mu = 70$). *Second row:* corresponding zoomed-in regions in the first row. *Third row:* performance comparison with different methods on House with $\sigma = 3$, *from left to right:* observed image, restored results by RMNU with $PSNR = 26.30dB$, FRSNU with $PSNR = 26.60dB$, PDTGV-Idiv with $PSNR = 26.41dB$, and the proposed method with $PSNR = 26.72dB$ ($\lambda = 0.5$, $\mu = 70$). *Bottom row:* corresponding zoomed-in regions in the third row

results, we observe that all methods improve the images quality well even the noise level is high. For better visualisation, we also present the zoomed-in local results in Figs. 2–4. From Figs. 2 and 3, one can see the despeckled results by RMNU, FRSNU are significantly degraded by staircase effects, especially in smooth regions, such as the cheek of Zelda and Face. However, our proposed method and PDTGV-Idiv process smooth regions better than RMNU, FRSNU. At the same time, our method and PDTGV-Idiv are able to keep the discontinuity around the lip and nose. In Fig. 4, one can observe that our method and PDTGV-Idiv are effective to recover smooth regions as well as discontinuities at object boundaries. Meanwhile, the smooth regions are recovered as piecewise constant regions by RMNU and FRSNU. The restored results by our method and PDTGV-Idiv are much visual pleasant. This illustrates that

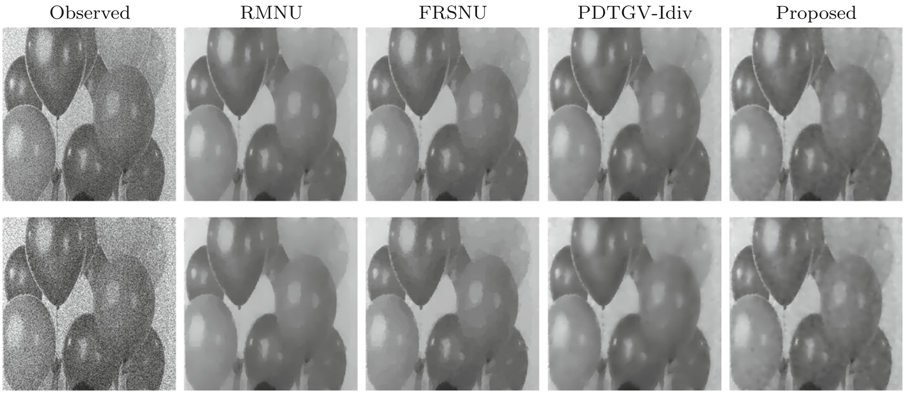

Fig. 5 *First row:* performance comparison of different methods on Pallon with $\sigma = 2$, *from left to right:* observed image, restored results by RMNU with $PSNR = 32.05dB$, FRSNU with $PSNR = 32.19dB$, PDTGV-Idiv with $PSNR = 32.32dB$, and the proposed method with $PSNR = 32.37dB$ ($\lambda = 0.8$, $\mu = 20$). *Second row:* performance comparison of different methods on Pallon with $\sigma = 3$, *from left to right:* observed image, restored results by RMNU with $PSNR = 29.62dB$, FRSNU with $PSNR = 30.28dB$, PDTGV-Idiv with $PSNR = 30.37dB$, and the proposed method with $PSNR = 30.45dB$ ($\lambda = 0.5$, $\mu = 20$)

the introduction of higher-order term in the denoising procedure produces higher quality.

It is interesting that we observe some isolated spots in the restored results by PDTGV-Idiv. This phenomena is also observed in the results presented in Figs. 5, 6 and 7. On the other hand, our method do not produce this artifact.

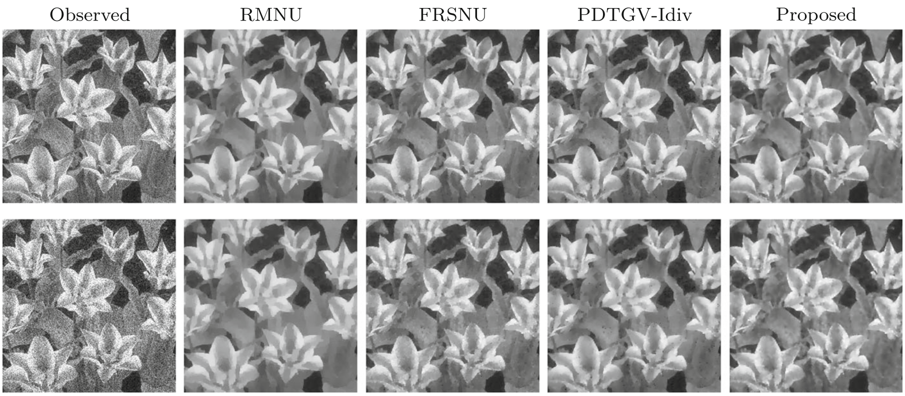

Fig. 6 *First row:* performance comparison of different methods on Tulip with $\sigma = 2$, *from left to right:* observed image, restored results by RMNU with $PSNR = 26.59dB$, FRSNU with $PSNR = 27.26dB$, PDTGV-Idiv with $PSNR = 27.20dB$, and the proposed method with $PSNR = 27.40dB$ ($\lambda = 1$, $\mu = 10$). *Second row:* performance comparison of different methods on Tulip with $\sigma = 3$, *from left to right:* observed image, restored results by RMNU with $PSNR = 24.45dB$, FRSNU with $PSNR = 25.33dB$, PDTGV-Idiv with $PSNR = 25.21dB$, and the proposed method with $PSNR = 25.57dB$ ($\lambda = 0.7$, $\mu = 10$)

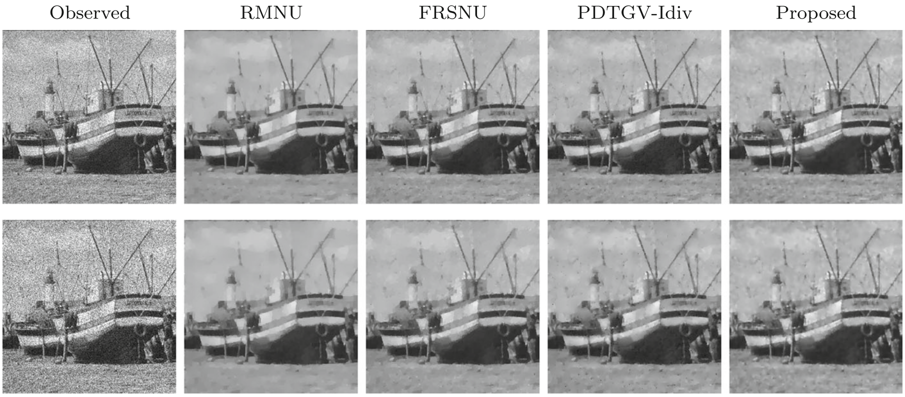

Fig. 7 *First row:* performance comparison of different methods on Barche with $\sigma = 2$, *from left to right:* observed image, restored results by RMNU with $PSNR = 27.54dB$, FRSNU with $PSNR = 27.87dB$, PDTGV-Idiv with $PSNR = 27.76dB$, and the proposed method with $PSNR = 27.96dB$ ($\lambda = 1.2$, $\mu = 10$). *Second row:* performance comparison of different methods on Barche with $\sigma = 3$, *from left to right:* observed image, restored results by RMNU with $PSNR = 25.64dB$, FRSNU with $PSNR = 25.96dB$, PDTGV-Idiv with $PSNR = 25.84dB$, and the proposed method with $PSNR = 26.17dB$ ($\lambda = 0.6$, $\mu = 50$)

Figures 5, 6 and 7 present the comparison between different methods on the images Pallon, Tulip, and Barche contaminated by the speckle noise with $\sigma = 2$ and $\sigma = 3$. One can similar observe that the staircase effects in flat regions are avoided by our method and PDTGV-Idiv such as the petals of Tulip in Fig. 6. In these experiments, our method achieves the highest SSIM values. Therefore, it is reasonable to conclude that our results are pleasant to the human eye. All these experiments show that our method is effective to remove speckle noise and alleviate staircase effects.

Table 1 summarizes the PSNR (in dB), SSIM and CPU time of the different methods on all testing images in Fig. 1 with $\sigma = 2$, $\sigma = 3$ and $\sigma = 4$. From Table 1, one can see that in most cases, our method generates a slightly higher PSNR, and SSIM than RMNU, FRSNU, and PDTGV-Idiv, indicating that our method is powerful in removing noise and preserving geometry. The computation time is quite competitive with other compared methods in most cases.

Test 2 We study the sensitivity of the number of inner iterations to be set in the proposed algorithm for solving the x-subproblem. We use the Face image contaminated by the noise with standard deviation $\sigma = 3$ as an example. Table 2 shows the PSNR values, SSIM values and computation time for different inner iteration number. From this table, we observed that when the iteration number becomes larger, the PSNR values and SSIM almost keep unchanged, but the computation time becomes much longer. We remark that the above observation is also valid for other testing images. From the discussion, we get that it is sufficient to set the number of inner iteration to be 2 for solving the x-subproblem.

Table 1 Comparison of the performance of the methods: RMNU, FRSNU, and PDTGV-Idiv in terms of PSNR, SSIM and CPU time (seconds)

σ	Image	RMNU PSNR/SSIM/Time	FRSNU PSNR/SSIM/Time	PDTGV-Idiv PSNR/SSIM/Time	Proposed PSNR/SSIM/Time
	Zelda	32.27/0.9224/26.8	32.78/0.9286/44.5	33.19/0.9364/16.1	*33.38/0.9381*/7.0
	Face	31.13/0.9022/6.8	31.35/0.8988/6.4	31.19/0.8792/3.8	*31.61/0.9185*/5.7
2	House	28.15/0.8837/28.4	28.35/*0.8881*/34.8	28.32/0.8732/16.7	*28.47*/0.8864/17.9
	Pallon	32.05/0.8799/5.3	32.19/0.8756/8.7	32.32/0.8806/3.3	*32.37/0.8847*/2.6
	Tulip	26.59/0.8007/6.4	27.26/0.8213/7.7	27.20/0.8172/3.0	*27.40/0.8282*/2.6
	Barche	27.54/0.7721/7.0	27.87/0.7817/7.1	27.76/0.7729/3.0	*27.96/0.7892*/2.0
	Zelda	29.90/0.8783/50.9	31.07/0.8965/66.9	*31.64*/0.9097/23.5	31.46/*0.9114*/9.5
	Face	29.09/0.8709/10.4	29.41/0.8682/9.5	29.12/0.8258/4.2	*29.53/0.8889*/8.1
3	House	26.30/0.8312/51.0	26.60/*0.8358*/52.7	26.41/0.8134/25.7	*26.72*/0.8317/27.1
	Pallon	29.62/0.8505/10.7	30.28/0.8478/13.4	30.37/0.8528/4.7	*30.45/0.8583*/3.5
	Tulip	24.45/0.7248/11.0	25.33/0.7555/11.9	25.21/0.7501/4.6	*25.57/0.7739*/2.7
	Barche	25.64/0.7061/10.2	25.96/0.7183/12.2	25.84/0.7103/4.7	*26.17/0.7311*/5.6
	Zelda	28.53/0.8569/60.6	29.62/0.8674/81.9	*30.49*/0.8823/30.9	30.01/*0.8940*/35.8
	Face	27.21/0.8451/18.1	27.98/0.8465/11.8	27.61/0.7670/6.1	*28.18/0.8660*/10.4
4	House	24.70/0.7793/83.5	25.33/0.7903/70.7	25.11/0.7582/33.7	*25.37/0.8062*/39.8
	Pallon	27.19/0.8217/17.4	28.69/0.8266/18.5	*29.17*/0.8304/6.0	28.71/*0.8441*/4.6
	Tulip	22.74/0.6549/16.4	23.97/0.7018/15.7	23.99/0.7016/6.3	*24.21/0.7251*/3.2
	Barche	24.28/0.6553/14.8	24.74/0.6704/15.1	24.65/0.6611/6.6	*24.90/0.6871*/7.9

The italicized entries represent the highest PSNR and SSIM for each test images

4.2 Experiments on real ultrasound images

In this section, we test the performance of the proposed method on some real ultrasound images and compare with FRSNU, PDTGV-Idiv. Since the performance of the RMNU depends on the estimation of the variance, we do not compare our method with the RMNU in this section. The denoising results on the real ultrasound thyroid nodules, the breast cancer mass image and the abdomen image are presented in Fig. 8. The second column shows the restoration results by FRSNU. We can see from the restored images that FRSNU method remove speckle noise effectively but at the

Table 2 Restoration results with different inner iteration number in proposed algorithm of Face with $\sigma = 3$

Iteration number	1	2	6	10	14	18	22
PSNR	29.53	29.53	29.54	29.54	29.54	29.54	29.54
SSIM	0.8887	0.8889	0.8889	0.8889	0.8889	0.8889	0.8889
Time	7.3	8.1	13.2	20.3	21.9	26.5	29.6

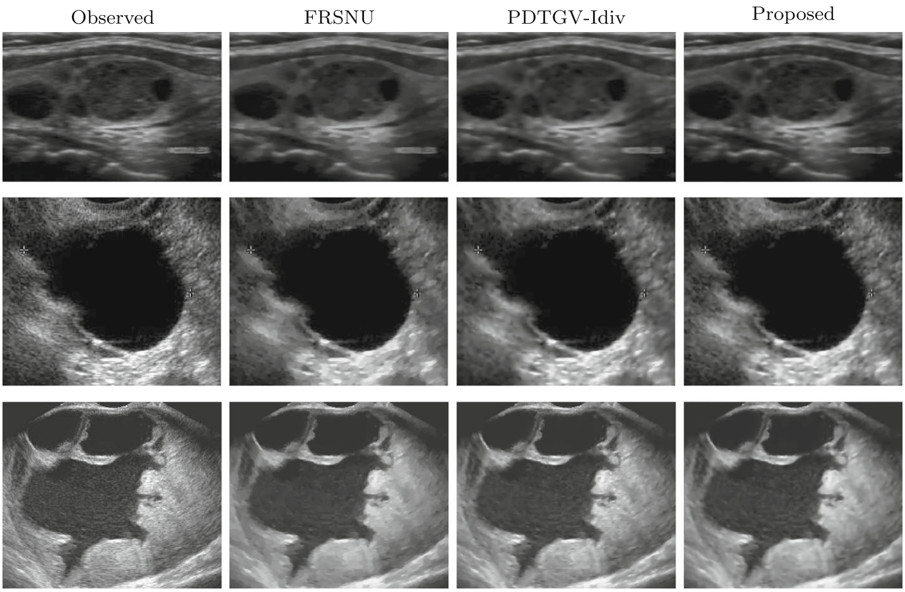

Fig. 8 Comparison with different methods on ultrasound images. *First column*, *from top to bottom:* a real ultrasound thyroid nodules image, a real breast cancer mass ultrasound image, a real ultrasound ovary cancer images; *second column to last column:* corresponding restoration results by FRSNU, PDTGV-Idiv and the proposed method

same time cause the staircase artifacts. However, our method and PDTGV-Idiv can suppress staircase effects.

5 Conclusions

We propose a new approach to suppress speckle noise in ultrasound images which combines the advantage of total variation and high-order total variation. We get the data fidelity term of the proposed model by using I-divergence. Then, we solve the proposed model by alternating direction method with multiplier and compare with three other competitive speckle removal methods. Numerical simulations show that the proposed method removes speckle noise quite well and overcomes staircase effect which is caused by total variation regularization. In our paper, we do not update the regularization parameters α and β during the iteration. Some adaptive techniques can be used to choose regularization parameters to get better restoration results.

Acknowledgements The authors would like to thank Meriem Hacini (Laboratoire d' Automatique et de Robotique, Algeria) for providing the real ultrasound images. This research is supported by 973 Program (2013CB329404), NSFC (61370147, 11401081, 61402082).

References

1. Abd-Elmoniem, K.Z., Youssef, A.-B.M., Kadah, Y.M.: Real-time speckle reduction and coherence enhancement in ultrasound imaging via nonlinear anisotropic diffusion. IEEE Trans. Biomed. Eng. **49**, 997–1014 (2002)
2. Bertero, M., Boccacci, P., Desiderà, G., Vicidomini, G.: Image deblurring with poisson data: from cells to galaxies. Inverse Probl. **25**, 123006 (2009)
3. Bredies, K., Kunisch, K., Pock, T.: Total generalized variation. SIAM J. Imaging Sci. **3**, 492–526 (2010)
4. Caiszar, I.: Why least squares and maximum entropy? an axiomatic approach to inference for linear inverse problems. Ann. Stat. **8**, 2032–2066 (1991)
5. Chambolle, A., Lions, P.-L.: Image recovery via total variation minimization and related problems. Numer. Math. **76**, 167–188 (1997)
6. Chen, Y., Huang, T.-Z., Deng, L.-J., Zhao, X.-L., Wang, M.: Group sparsity based regularization model for remote sensing image stripe noise removal. Neurocomputing. doi:10.1016/j.neucom.2017.05.018, http://www.sciencedirect.com/science/article/pii/S0925231217308287 (2017)
7. Chen, Y., Huang, T.-Z., Zhao, X.-L., Deng, L.-J., Huang, J.: Stripe noise removal of remote sensing images by total variation regularization and group sparsity constraint. Remote Sens. **9**(559). doi:10.3390/rs9060559 (2017)
8. Coupé, P., Hellier, P., Kervrann, C., Barillot, C.: Nonlocal means-based speckle filtering for ultrasound images. IEEE Trans. Image Process. **18**, 2221–2229 (2009)
9. Deledalle, C.-A., Denis, L., Tupin, F.: Iterative weighted maximum likelihood denoising with probabilistic patch-based weights. IEEE Trans. Image Process. **18**, 2661–2672 (2009)
10. Devi, P.N., Asokan, R.: An improved adaptive wavelet shrinkage for ultrasound despeckling. Sadhana **39**, 971–988 (2014)
11. Eckstein, J., Bertsekas, D.P.: On the Douglas-Rachford splitting method and the proximal point algorithm for maximal monotone operators. Math. Program. **55**, 293–318 (1992)
12. Feng, W., Lei, H., Gao, Y.: Speckle reduction via higher order total variation approach. IEEE Trans. Image Process. **23**, 1831–1843 (2014)
13. Gabay, D., Mercier, B.: A dual algorithm for the solution of nonlinear variational problems via finite element approximation. Comput. Math. Appl. **2**, 17–40 (1976)
14. Hacini, M., Hachouf, F., Djemal, K.: A new speckle filtering method for ultrasound images based on a weighted multiplicative total variation. Signal Process. **103**, 214–229 (2014)
15. Hansen, P.C., Nagy, J.G., O'leary, D.P.: Deblurring images: matrices, spectra, and filtering. SIAM (2006)
16. He, B., Liao, L.-Z., Han, D., Yang, H.: A new inexact alternating directions method for monotone variational inequalities. Math. Program. **92**, 103–118 (2002)
17. He, B., Tao, M., Yuan, X.: Alternating direction method with Gaussian back substitution for separable convex programming. SIAM J. Optimiz. **22**, 313–340 (2012)
18. He, B., Yang, H.: Some convergence properties of a method of multipliers for linearly constrained monotone variational inequalities. Oper. Res. Lett. **23**, 151–161 (1998)
19. Huang, J., Yang, X.: Fast reduction of speckle noise in real ultrasound images. Signal Process. **93**, 684–694 (2013)
20. Huang, Y.-M., Ng, M.K., Wen, Y.-W.: A new total variation method for multiplicative noise removal. SIAM J. Imaging Sci. **2**, 20–40 (2009)
21. Ji, T.-Y., Huang, T.-Z., Zhao, X.-L., Ma, T.-H., Deng, L.-J.: A non-convex tensor rank approximation for tensor completion. Appl. Math. Model. **48**, 410–422 (2017)
22. Jin, Z., Yang, X.: A variational model to remove the multiplicative noise in ultrasound images. J. Math. Imaging Vis. **39**, 62–74 (2011)
23. Khare, A., Khare, M., Jeong, Y., Kim, H., Jeon, M.: Despeckling of medical ultrasound images using Daubechies complex wavelet transform. Signal Process. **90**, 428–439 (2010)
24. Krissian, K., Kikinis, R., Westin, C.-F., Vosburgh, K.: Speckle-constrained filtering of ultrasound images. CVPR. **2**, 547–552 (2005)
25. Krissian, K., Vosburgh, K., Kikinis, R., Westin, C.-F.: Anisotropic Diffusion of Ultrasound Constrained by Speckle Noise Model. Laboratory of Mathematics in Imaging, Harvard Medical School, Technical Report (2004)

26. Kuan, D.T., Sawchuk, A.A., Strand, T.C., Chavel, P.: Adaptive restoration of images with speckle. IEEE Trans. Acoust. Speech. **35**, 373–383 (1987)
27. Lefkimmiatis, S., Bourquard, A., Unser, M.: Hessian-based norm regularization for image restoration with biomedical applications. IEEE Trans. Image Process. **21**, 983–995 (2012)
28. Li, F., Ng, M.K., Shen, C.: Multiplicative noise removal with spatially varying regularization parameters. SIAM J. Imaging Sci. **3**, 1–20 (2010)
29. Li, F., Shen, C., Fan, J., Shen, C.: Image restoration combining a total variational filter and a fourth-order filter. J. Vis. Commun. Image. R. **18**, 322–330 (2007)
30. Liu, J., Huang, T.-Z., Selesnick, I.W., Lv, X.-G., Chen, P.-Y.: Image restoration using total variation with overlapping group sparsity. Inf. Sci. **295**, 232–246 (2015)
31. Lopes, A., Touzi, R., Nezry, E.: Adaptive speckle filters and scene heterogeneity. IEEE Trans. Geosci. Remote Sens. **28**, 992–1000 (1990)
32. Loupas, A.: Digital image processing for noise reduction in medical ultrasonics. PhD thesis, University of Edinburgh, UK (1988)
33. Loupas, T., McDicken, W., Allan, P.: An adaptive weighted median filter for speckle suppression in medical ultrasonic images. IEEE Trans. Circuits Syst. **36**, 129–135 (1989)
34. Lysaker, M., Lundervold, A., Tai, X.-C.: Noise removal using fourth-order partial differential equation with applications to medical magnetic resonance images in space and time. IEEE Trans. Image Process. **12**, 1579–1590 (2003)
35. Lysaker, M., Tai, X.-C.: Iterative image restoration combining total variation minimization and a second-order functional. Int. J. Comput. Vision. **66**, 5–18 (2006)
36. Marks, D.L., Ralston, T.S., Boppart, S.A.: Speckle reduction by I-divergence regularization in optical coherence tomography. JOSA A. **22**, 2366–2371 (2005)
37. Mei, J.-J., Dong, Y.-Q., Huang, T.-Z., Yin, W.-T.: Cauchy noise removal by nonconvex ADMM with convergence guarantees. J. Sci. Comput. doi:10.1007/s10915-017-0460-5 (2017)
38. Michailovich, O.V., Tannenbaum, A.: Despeckling of medical ultrasound images. IEEE Trans. Ultrason., Ferroelect., Freq. Contr. **53**, 64–78 (2006)
39. Ng, M.K., Chan, R.H., Tang, W.-C.: A fast algorithm for deblurring models with neumann boundary conditions. SIAM J. Sci. Comput. **21**, 851–866 (1999)
40. Papafitsoros, K., Schönlieb, C.-B.: A combined first and second order variational approach for image reconstruction. J. Math. Imaging Vis. **48**, 308–338 (2014)
41. Parrilli, S., Poderico, M., Angelino, C.V., Verdoliva, L.: A nonlocal SAR image denoising algorithm based on LLMMSE wavelet shrinkage. IEEE Trans. Geosci. Remote Sens. **50**, 606–616 (2012)
42. Resmerita, E., Engl, H.W., Iusem, A.N.: The expectation-maximization algorithm for ill-posed integral equations: a convergence analysis. Inverse Probl. **23**, 2575 (2007)
43. Rudin, L., Lions, P.-L., Osher, S.: Multiplicative denoising and deblurring: theory and algorithms. In: Geometric Level Set Methods in Imaging, Vision, and Graphics, pp. 103–119 (2003)
44. Setzer, S., Steidl, G.: Variational methods with higher order derivatives in image processing. Approximation **12**, 360–386 (2008)
45. Shi, B., Huang, L., Pang, Z.-F.: Fast algorithm for multiplicative noise removal. J. Vis. Commun. Image R. **23**, 126–133 (2012)
46. Slabaugh, G., Unal, G., Fang, T., Wels, M.: Ultrasound-specific segmentation via decorrelation and statistical region-based active contours. CVPR. **1**, 45–53 (2006)
47. Steidl, G., Teuber, T.: Removing multiplicative noise by Douglas-Rachford splitting methods. J. Math. Imaging Vis. **36**, 168–184 (2010)
48. Tur, M., Chin, K.C., Goodman, J.W.: When is speckle noise multiplicative? Appl. Opt. **21**, 1157–1159 (1982)
49. Tuthill, T., Sperry, R., Parker, K.: Deviations from Rayleigh statistics in ultrasonic speckle. Ultrason. Imaging **10**, 81–89 (1988)
50. Wang, S., Guo, W., Huang, T.-Z., Raskutti, G.: Image inpainting using reproducing kernel Hilbert space and Heaviside function variations. J. Comput. Appl. Math. **311**, 551–564 (2017)
51. Wang, Z., Bovik, A.C., Sheikh, H.R., Simoncelli, E.P.: Image quality assessment: from error visibility to structural similarity. IEEE Trans. Image Process. **13**, 600–612 (2004)
52. Wu, C., Tai, X.-C.: Augmented Lagrangian method, dual methods, and split Bregman iteration for ROF, vectorial TV, and high order models. SIAM J. Imaging Sci. **3**, 300–339 (2010)
53. You, Y.-L., Kaveh, M.: Fourth-order partial differential equations for noise removal. IEEE Trans. Image Process. **9**, 1723–1730 (2000)

54. Yu, J., Tan, J., Wang, Y.: Ultrasound speckle reduction by a SUSAN-controlled anisotropic diffusion method. Pattern Recogn. **43**, 3083–3092 (2010)
55. Zhao, X.-L., Wang, F., Huang, T.-Z., Ng, M.K., Plemmons, R.J.: Deblurring and sparse unmixing for hyperspectral images. IEEE Trans. Geosci. Remote Sens. **51**, 4045–4058 (2013)
56. Zhao, X.-L., Wang, F., Ng, M.K.: A new convex optimization model for multiplicative noise and blur removal. SIAM J. Imaging Sci. **7**, 456–475 (2014)